

Unsupervised Sparse Pattern Diagnostic of Defects With Inductive Thermography Imaging System

Bin Gao, *Senior Member, IEEE*, Wai Lok Woo, *Senior Member, IEEE*, Yunze He, *Member, IEEE*, and Gui Yun Tian, *Senior Member, IEEE*

Abstract—This paper proposes an unsupervised method for diagnosing and monitoring defects in inductive thermography imaging system. The proposed method is fully automated and does not require manual selection from the user of the specific thermal frame images for defect diagnosis. The core of the method is a hybrid of physics-based inductive thermal mechanism with signal processing-based pattern extraction algorithm using sparse greedy-based principal component analysis (SGPCA). An internal functionality is built into the proposed algorithm to control the sparsity of SGPCA and to render better accuracy in sizing the defects. The proposed method is demonstrated on automatically diagnosing the defects on metals and the accuracy of sizing the defects. Experimental tests and comparisons with other methods have been conducted to verify the efficacy of the proposed method. Very promising results have been obtained where the performance of the proposed method is very near to human perception.

Index Terms—Data analytics for diagnosis and monitoring, inductive thermal imaging, instrumentation, machine intelligence, nondestructive testing and evaluation (NDT&E).

Manuscript received January 20, 2015; revised April 17, 2015; accepted June 10, 2015. Date of publication October 26, 2015; date of current version February 02, 2016. This work was supported by the National Natural Science Foundation of China under Grant 51377015, Grant F011404, Grant 61401071, and Grant 61527803; in part by NSF under Grant U1430115; in part by the FP7 HEMOW IRSES project 269202; in part by the China Postdoctoral Science Foundation under Grant 136413; in part by the Science and Technology Department of Sichuan Province, China, under Grant 2013HH0059; and in part by the Fundamental Research Funds for the Central Universities under Grant ZYGX2014J068. Paper no. TII-15-0092.

B. Gao is with the School of Automation Engineering, University of Electronic Science and Technology of China, Chengdu 611731, China (e-mail: bin_gao@uestc.edu.cn).

W. L. Woo is with the School of Electrical and Electronic Engineering, Newcastle University, Newcastle Upon Tyne NE1 7RU, U.K. (e-mail: w.l.woo@ncl.ac.uk).

Y. He is with the College of Mechatronics Engineering and Automation, National University of Defense Technology (NUDT), Changsha 410073, China (e-mail: hejicker@163.com).

G. Y. Tian is with the School of Automation Engineering, University of Electronic Science and Technology of China, Chengdu 611731, China, and also with the School of Electrical and Electronic Engineering, Newcastle University, Newcastle Upon Tyne NE1 7RU, U.K. (e-mail: g.y.tian@ncl.ac.uk).

Color versions of one or more of the figures in this paper are available online at <http://ieeexplore.ieee.org>.

Digital Object Identifier 10.1109/TII.2015.2492925

I. INTRODUCTION

IMAGING diagnostic system for defect detection is highly demanded in industry [1], [2]. This has been applied on inspection of electronic chips or dies in semiconductor production lines [3]. Acciani *et al.* extracted the features of the regions of interest in test images and then built multilayer neural networks for defect detection [4] on solder joints in surface mount technology of industry. Tsai *et al.* proposed defect inspection system of solar modules in electroluminescence (EL) images [5]. Picon *et al.* proposed fuzzy spectral and spatial feature integration method for classification of nonferrous materials in hyperspectral data [6]. All these methods recognize that image-based defect diagnostic system is a wide group of analysis technique used in science and industry to evaluate the properties of material, component, or system without causing damage [7]–[9]. Infrared thermography systems have reached a prominent status as a nondestructive testing and evaluation (NDT&E) image diagnostic method [10]–[12] with the advantages of being fast, and providing noncontact, noninteraction, real-time measurements over a large detection area with a long range, security of personnel, and relatively easy interpretation of results. Infrared thermography can be used to assess and predict the structure or behavior beneath the surface by measuring the distribution of infrared radiation and converting the measurements into a temperature scale.

Inductive thermography (IT) system which combines two techniques: 1) Eddy current (EC); and 2) thermography [13] has the potential with an increasing span of applications [14]. Comparing with other thermography NDT&E systems, the heat of IT is not limited to the sample surface, rather it can reach a certain depth, which governed by the skin depth of EC. Furthermore, IT focuses the heat on the defect due to friction or EC distortion, which increases the temperature contrast between the defective region and defect-free areas. Eddy current pulsed thermography (ECPT) is a kind of IT method, which is the most widely used such as penetration depths measurement in metallic materials [15], small defects detection for compressor blades [16], probability of detection (POD) estimation [17] of fatigue cracks, impact evaluation in carbon fiber reinforced plastic (CFRP) [18], corrosion and blister detection under coating [19], and multiple cracks detection [20]. All these works require signal processing tools to do defects analysis. In ECPT, several thermal transient response features have been used as an indicator of defect status, which is critical

for acceptance/rejection decisions for maintenance and life-time prediction [21]. Most methods are limited on manually selecting the proper contrast components. To enhance the flaw contrast and improve noise rejection qualities, pattern-based image enhancement has been conducted by introducing the raw data upon a set of orthogonal basis functions. Fourier transform was applied to pulsed thermography and enhanced the flaw contrast significantly using phase map [22]. Influence of nonuniform heating and surface emissivity variation was removed by using a Fourier transformation-based image reconstruction algorithm [23]. Instead of a prescribed set of basis functions, empirical orthogonal functions were also employed to maximize the anomalous patterns of transient response. The efficiency of principal component analysis (PCA) was compared on thermography features extraction by considering the initial sequence as either a set of images or a set of temporal profiles [24]. In addition, the independent component analysis (ICA) [25], [26] and nonnegative matrix factorization (NMF) [27], [28] are proposed for defect characterization in IT system. However, most pattern extraction-based methods are only employed as a signal processing tool. The physics mechanism is not fully linked to provide the benefits of defect detection, while the results are acceptable, they are not completely accurate. This ambiguous case prevents the use of IT system in automated environments.

The sparse modeling of signals [29]–[36] which has proven to be effective in signal processing, denoising, deconvolution, compressive sensing reconstruction, inpainting, data mining, multimedia, NMF, etc. Most natural signals exhibit such sparsity property in adequately chosen signal representations. These include the wavelets [37], the curvelets [38], or even adaptively learned signal representations [39]. Greedy algorithms [40] have been widely used to find approximate solutions quickly to combinatorial optimization problems [41]. In a few cases, optimal solutions are guaranteed. Greedy algorithms for sparse approximation have inspired less adaptive methods. Matching pursuit (MP) can be converted to a low complexity adaptive form, as done in [42], and been extended to orthogonal MP (OMP) [43] as well as stage-wise OMP [44]. Compared with convex relaxation algorithms, greedy pursuits need more measurements, but they tend to be more computationally efficient. Sparsity has been exploited in recent unsupervised pattern recognition methods [45]–[48]. The group of research interest focuses on the low-rank and sparse components via convex optimization have also been attractive, the robust PCA, is [49] proposed iterative thresholding methods with low complexity, but with low speed of convergence. Lin *et al.* [49] proposed accelerated proximal gradient (APG) methods which are faster and more accurate than robust PCA. The latest approach such as variational Bayesian and Markov chain Monte Carlo (MCMC)-based sparse PCA with specific prior where the model parameters and hyperparameters are adapted by using [50] and [51]. In all cases, a fully Bayesian treatment is applied to inference. While these approaches increase the accuracy of specific application and works efficient when suitable priority is selected. Moreover, it consumes significantly high computational complexity at each iteration to adapt the parameters and its hyperparameters.

The contributions of the current work lie in the development of the physics mechanism that underlies the IT system and a derivation of a mathematical model that bridges the gap between the physics mechanism and signal processing analysis. The aim is to develop a data-analytics algorithm to extract anomalous patterns in the IT system. A physics-based signal processing approach combining sparse greedy principal component analysis (SGPCA) is developed to identify and search the defect region in the sample. The model represents a low-rank variable as a sparse bilateral factorization with greedy-based optimization to reduce the computational complexity during the sparse pattern extraction stage. The physics mechanism as to why sparse information benefits the IT heating phase will also be discussed in detail. The comparison in terms of the POD and computational complexity has been undertaken for different sparse pattern extraction algorithms through the real experiments. Experimental tests on man-made metal defects and natural defects with complex geometry have been conducted to show the validity of the proposed algorithm.

This paper is organized as follows. Section II discusses the physics model of IT mechanism and the linkage as well as development of sparse pattern extraction algorithm. Section III describes the proposed sparse thermal pattern extraction method. Sections IV and V introduce the experimental setup and present the experiment results. Finally, Section VI concludes the work.

II. PROPOSED METHODOLOGY

A. Physics Mechanism of IT System

1) *Inductive Thermal Conduction*: The infrared camera records both the spatial and the transient response of temperature variation on the specimen. This can be represented as a spatial-transient tensor $\bar{\mathbf{Y}}$, which has dimension $\underbrace{N_x \times N_y}_{\text{Spatial}} \times \underbrace{N}_{\text{Transient}}$. The governing equation describing the EM field in the ECPT system can be deduced from Maxwell's equations. When an EM field is applied to a conductive material, the temperature increases owing to resistive heating from the induced electric current, which is known as Joule heating. The sum of the generated resistive heat Q is proportional to the square of the magnitude of the electric current density. Current density, in turn, is proportional to the electric field intensity vector $\vec{\mathbf{E}}$. The following equation expresses this relationship:

$$Q = \frac{1}{\sigma} |\vec{\mathbf{j}}_s|^2 = \frac{1}{\sigma} |\sigma \vec{\mathbf{E}}|^2, \quad \text{where } \sigma = \frac{\sigma_0}{1 + \alpha(T - T_0)} \quad (1)$$

σ is dependent on temperature, σ_0 is the conductivity at the reference temperature T_0 , and α is the temperature coefficient of resistivity, which describes how resistivity varies with temperature. In general, by taking account of heat diffusion and Joule heating [24], the heat conduction equation of a specimen can be expressed as

$$\frac{\partial T}{\partial t} = \frac{k}{\rho C_p} \left(\frac{\partial^2 T}{\partial x^2} + \frac{\partial^2 T}{\partial y^2} + \frac{\partial^2 T}{\partial z^2} \right) + \frac{1}{\rho C_p} q(x, y, z, t) \quad (2)$$

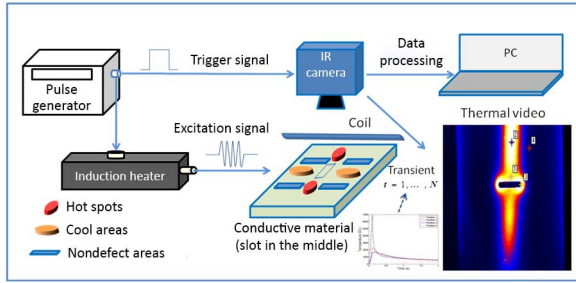


Fig. 1. ECPT system.

where $T = T(x, y, z, t)$ is the temperature distribution, k is the thermal conductivity of the material ($\text{W/m} \cdot \text{K}$), which is dependent on temperature. ρ is the density (kg/m^3), C_p is specific heat ($\text{J/kg} \cdot \text{K}$). $q(x, y, z, t)$ is the internal heat generation function per unit volume, which is the result of the EC excitation. The variation of temporal temperature depends on the spatial temperature variation for heat conduction. According to (2), heat conduction is influenced by $T(x, y, z, t)$, ξ , v , σ , μ , and l , where ξ denotes the sensor geometry factor; v denotes the parameters of the excitation (frequency and amplitude) and l denotes the lift off (distance between the sensor and sample). From the above analysis, it becomes clear that the variation of temperature spatially and its transient response recorded from the IR camera directly reveals the intrinsic properties variation of the conductive material.

2) IT Defect Detection: Fig. 1 shows the diagram of IT defect detection system. The excitation signal generated by the excitation module is a small period of high-frequency current. The current in the coil will induce the ECs and generate the resistive heat in the conductive material. The heat will diffuse in time until the heat reaches equilibrium in the material. If a defect (e.g., crack and fatigue region) is present in the conductive material, EC distribution as well as heat diffusion process will vary. Consequently, the spatial distribution of temperature on the surface of material and the temperature transient response will show the variation, which is captured by an infrared camera. It can be divided into two phases: 1) heating phase; and 2) cooling phase. As an example, we take a finite length sample with small penetrated slot as a defect testing sample. The resultant heating frame from IT (0.1 s) is presented in Fig. 1 right bottom panel. In the heating phase, different heat generation rates enlarge the temperature spatial variation. Hot spots are observed around the slot tips and the cool areas locate at both sides of the slot. In the cooling phase, heat diffuses from high-temperature area to low-temperature area, and reduces the contrast. In addition, the area located far away from excitation coil will continually rise temperature because of its heat diffusion. These different areas can be considered as the pattern regions which share the similar transient responses in the sample. The infrared camera functioned as a temperature spatial image signal recorder along with time flowing. In addition, the camera actually records the mixed image signal corresponding to the signal image from the thermal pattern regions at each time point. These regions are termed as thermal patterns in IT.

The hot spots are used specially for defect location and sizing. Fig. 1 shows the example of temperature distribution at the

sample surface as the lift-off distance is set $d = 4$ mm. When the inductor is close to the tip of the defect ($d = 4$ mm), it is seen that significant EC flows around the tip of the defect and the defect behaves predominantly as a slot.

3) Relationship Between Excitation System, Heating Phase, and Cooling Phase With Respect to Material Variation: IT uses inductive heater as the excitation system. Hence, it is specific for conductive materials or multilayer system with conductive layer. The inductive heat depends on the parameters of material and excitation signal.

- 1) To optimize the signal-to-noise ratio (SNR), the heat power should be maximized. Normally, the high-current amplitude (hundreds of ampere) and great frequency (>100 kHz) are used.
- 2) The longer heating time results in the accumulation of large amount of heat Q . For detecting surface defects, the long heating time is useful for good SNR and contrast [18]. At the same time, the longer heating time is useful for detecting the deep defects due to heat conduction from surface to deep defects [51].
- 3) The long cooling time is useful for heat conduction to detect deep defects. The thermal penetration depth for a pulsed excitation is determined by the thermal diffusivity α of the material and by the observation time t (cooling time) after pulse heating.
- 4) The small electrical conductivity can lead to a high heat power and great EC penetration depth. The thermal diffusivity depends on thermal conductivity, mass density and specific heat. If the thermal diffusivity is large, the temperature changes quickly. Hence the sampling frequency of the camera must be high enough to capture the changes of temperature.

4) Detectability: In general, the ECPT is valid for both deep and shallow defects, which is based on the physics principles of inductive heating, heat conduction, and infrared radiation. According to skin effect in inductive heating, the EC has a penetration depth δ , which is expressed by equation $\delta = \frac{1}{\sqrt{f\pi\mu\sigma}}$, where f is the frequency of the pulsed excitation. If the shallow defects are in this skin area, they will disturb the EC distribution and then the temperature distribution. Theoretically, the lower excitation frequency has deeper detection depth. In practice, in order to improve the heating efficient with IT, the frequency is about 100 kHz and the skin depth is relative small. For example, ferromagnetic metals have a much smaller skin depth (about 0.04 mm at 100 kHz). Therefore, shallow/surface defects can be detected. The heat will conduct to the interior and lateral area of the material. If the deep defects disturb the heat conduction process, the surface temperature distribution will be different from the surrounding area. The heat conduction is used to detect the deep defects [51]. The temperature will be captured by IR camera. If the surface defects show a different emissivity value, the temperature will be different from the surrounding area.

5) IT Multiphase Analysis: According to (2), the first-order derivative of the temperature response of transient response, as shown in Fig. 2(b), is composed of heat diffusion and Joule heating [52]. In Fig. 2(c), we can infer from the thermal video that the heat conduction procedure can be divided into six phases.

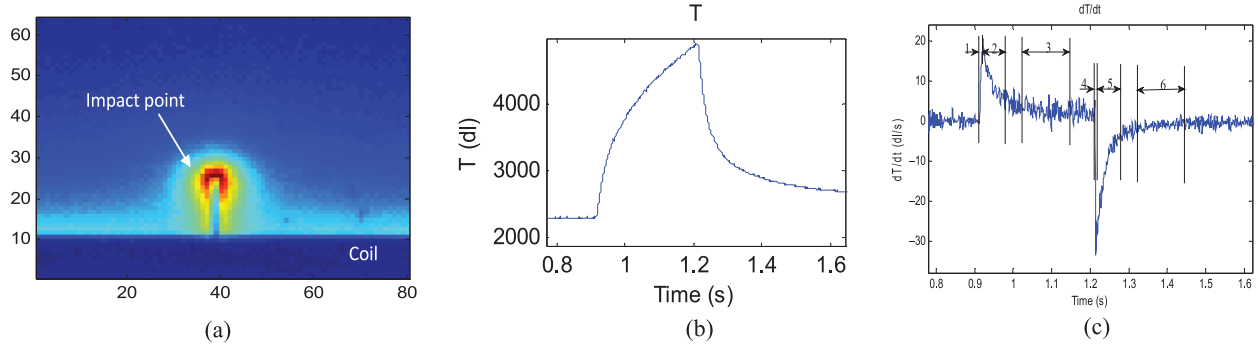


Fig. 2. (a) Thermal image at 0.1 s after heating. (b) Transient temperature response at impact point plotted against time. (c) First derivatives of temperature response.

- 1) Phase 1: A resultant singular electric current field is generated, and the EC quickly rises from zero to maximum, and then converges to a steady state. This phase is very short (approximately 5 ms) and the heat diffusion does not play an obvious role which can be considered zero or a constant small value. In (2), we only take into account the Joule heating during this phase.
- 2) Phase 2: Electric current field maintains a stable state. The sum of the generated resistive heat Q is constant. However, heat diffusion velocity gradually increases and following a different temperature increases according to Fourier's law of heat conduction. Simultaneously, heat diffusion is getting more obvious due to the significant heating propagation time. Heat diffusion plays a main role in the thermal video during this phase.
- 3) Phase 3: Heat conduction also reaches the equilibrium state. The sum of the generated resistive heat Q and heat diffusion are at equilibrium in this phase.
- 4) Phase 4: EC quickly decreases from maximum to zero when exciting signal is stopped. Similar to the first phase, the procedure is very short, which lasts about 5 ms. Change of heat diffusion is not abrupt in such a short time. Joule heating plays a main role in the thermal video during this phase.
- 5) Phase 5: There is no EC in this phase, so $q(x, y, z, t)$ can be omitted in (2). The change of the first-order derivative is resulted from the velocity variation of heat diffusion.
- 6) Phase 6: Heat diffusion is at a stable state.

As mentioned in Section I, IT focuses the heat on the defect due to friction and EC distortion, which increases the temperature contrast. Thus, for surface defects, the selection of phase one and four are directly attributed to Joule heating due to the EC distortion. More description and comparison of phase selection will be detailed in Section V. Moreover, the IR camera used as a temperature measurement sensor has an important role in IT. Inductive thermograph is a relative measurement technique, the temperature contrast between defect and surrounding area is important. Therefore, the sensitivity of camera has an influence on defect detect sensitivity. In the proposed method, the high-end thermal camera is used, the SC7500 is a Stirling cooled camera with a 320×256 array of $1.5\text{--}5 \mu\text{m}$ InSb detectors. This camera has a sensitivity of <20 mK and a maximum full frame rate of 383 Hz such that the interface of the camera sensitivity can be reduced to minima. The distance has an

influence on the heating efficiency. A small distance is desirable, but with an overly too small distance, the distribution of the EC is forced into a small area, which reduces the detectable area. To avoid this effect, transmission mode where IR camera and heater are located on the opposite side of objects is investigated if the object is thin. The increase of distance may decrease the SNR and defect detectability. In the proposed method, the 1 mm distance lift off between the coil and sample is verified to balance good SNR and proper excitation heating.

III. PHYSICS-BASED DATA ANALYTICS

A. Thermography Sparse Pattern Extraction

1) *Observation Model:* As shown in Fig. 1, hot spots are observed around the slot tips and the cool areas locate at both sides of the slot. In the cooling phase, heat diffuses from high temperature area to low temperature area, and reduces the contrast. In addition, the area where locate far away from excitation coil will continually rising temperature because of heat diffusion. These different areas can be considered as the thermal pattern regions. Specifically, it can be seen in Fig. 1, position 1 represents an hot spots region $\mathbf{X}_1(t)$ with high rising and high falling rate of temperature; position 2 represents an cool areas $\mathbf{X}_2(t)$ with moderate rising and falling rate; position 3 represents an nondefect region $\mathbf{X}_3(t)$ with high rising rate followed by a continually low speed rising and then drop down; and position 4 represents an nonexcitation region $\mathbf{X}_4(t)$ with continually temperature increasing. Mathematically, the thermography image captured by the infrared camera is considered as a mixing observation signal image $\mathbf{Y}(t)$. The term m_i is the mixing parameter which describes the contribution of the i th position to the induced recorded thermography image in Fig. 1. Thus, the mathematical model [25] can be described as

$$\mathbf{Y}(t) \approx \sum_{i=1}^{N_s} m_i \mathbf{X}_i(t) \quad (3)$$

where N_s denotes the number of independent signal image areas. The visual representation of (3) is shown in Fig. 3.

Our previous study [25] has developed single channel blind source separation algorithm for pattern separation of IT. However, the method requires statistical independence on the waveform within the duration of signal capture and further process of pattern identification is also demanded

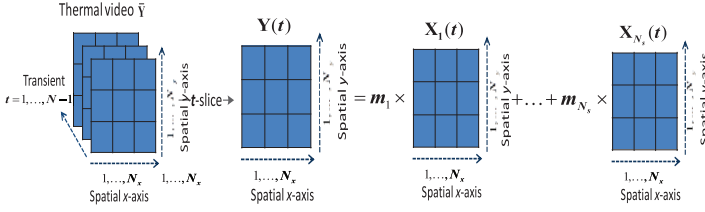


Fig. 3. Mathematical representation of mixing process of ECPT.

which is often violated in practice. Instead, we use a fixed-length segment drawn from transient response [53], [54], such that continuous transient slices of length N can be chopped out of a set of image sequences from t to $t + N - 1$, and the subsequent segment is denoted as $\mathbf{Y}' = [\text{vec}(\mathbf{Y}(t)), \text{vec}(\mathbf{Y}(t+1)), \dots, \text{vec}(\mathbf{Y}(t+N-1))]^T$, where “ \mathbf{T} ” denotes the transpose operator and “ vec ” denotes the vectorize operator. The constructed image sequences is then expressed as a linear combination of the signals generated by the different pattern regions such that

$$\mathbf{Y}' = \mathbf{M}\mathbf{X}' \quad (4)$$

where $\mathbf{Y}' \in R^{N \times L}$, $L = N_x \times N_y$. $\mathbf{M} = [\mathbf{m}_1, \dots, \mathbf{m}_{N_s}] \in R^{N \times N_s}$ is the mixing matrix, \mathbf{m}_i is the i th mixing vector and $\mathbf{X}' = [\text{vec}(\mathbf{X}_1(t)), \text{vec}(\mathbf{X}_2(t)), \dots, \text{vec}(\mathbf{X}_{N_s}(t))]^T \in R^{N_s \times L}$. Assuming that $N_s = N$ and \mathbf{M} has full rank.

2) General Principle of Pattern Extraction: Our previous study already used general PCA to separate the observed variables. To solve (4), one possible way is to use the singular value decomposition (SVD) which is a form of factorization

$$\mathbf{Y}' = \mathbf{U}\mathbf{\Sigma}\mathbf{V} \quad (5)$$

where \mathbf{U} and \mathbf{V} are the orthogonal matrices and $\mathbf{\Sigma}$ consist of the singular values. The columns of \mathbf{U} represent the PCA basis vectors. With possible dimension reduction, e.g., choosing $N_s \leq N$, there exists N_s number of basis vectors maximally informative subspace of input data, thus the basis vectors are selected and determined by the information contained in the nonzero singular values.

3) Sparse Pattern Extraction: However, previous study does not involve or leverage on the phases of heat conduction and sparse factors. Sparseness refers to a representational scheme where only a few units (out of a large population) are effectively used to represent typical data vectors [55]. In effect, this implies most units taking values close to zero while only few take significantly nonzero values. The sparse factors enforce the solution to consider only the significant region where the defect may lie within the surrounding background. This is shown in Fig. 2(a). For data with sparse outliers or partially contaminated by noise of overwhelming magnitude, sheer low-rank assumption cannot fully capture its complex structure. Therefore, (4) can be considered as combination of sparse pattern (e.g., hot spots) and nonsparse patterns

$$\mathbf{Y}' = \underbrace{[\mathbf{M}\mathbf{X}']_{i=1, \dots, N_s, i \neq j}}_{\mathbf{L}} + \underbrace{\mathbf{M}_j \mathbf{X}'_j}_{\mathbf{S}} + \mathbf{G}. \quad (6)$$

In reality, they play an important role in enhancing the defect detectability of IT system. A general assumption of (6) can be

denoted as $\mathbf{Y}' = \mathbf{L} + \mathbf{S} + \mathbf{G}$, i.e., the pattern matrix \mathbf{Y}' can be decomposed as the sum of a low-rank matrix \mathbf{L} (e.g., for position 2, 3, and 4 reflected patterns in Fig. 1), a sparse pattern \mathbf{S} (e.g., hot spots) which contains the spiky anomalies that are rarely shared by different instances, and \mathbf{G} which is the noise term. When the algorithm optimizes the sparse \mathbf{S} , it is actually trying to find the joint sparse estimation of \mathbf{M}_j and \mathbf{X}'_j (not just \mathbf{X}'_j). The sparse estimation of \mathbf{X}'_j is required to obtain the correct shape of the pattern while the sparse estimation of \mathbf{M}_j is to enable the user to determine the exact time when the target pattern takes place. By replacing \mathbf{L} with its bilateral factorization $\mathbf{L} = \mathbf{U}\mathbf{V}$ where \mathbf{U} and \mathbf{V} are rank-1 matrices of (6) (The low-rank matrix variable in solving other thermal patterns is modeled in a bilateral factorization form $\mathbf{U}\mathbf{V}$ for the purpose of developing SVD-free algorithms.) and regularizing the L_1 -norm of \mathbf{S} entries, the cost function can be expressed as

$$\min_{\mathbf{U}, \mathbf{V}, \mathbf{S}} \|\mathbf{Y}' - \mathbf{U}\mathbf{V} - \mathbf{S}\|_F^2 + \lambda \|\text{vec}(\mathbf{S})\|_1 \quad (7)$$

where $\text{vec}(\cdot)$ denotes the vectorize operation, $\|\cdot\|_F$ denotes the Frobenius norm, and $\|\cdot\|_1$ denotes L_1 -norm. In this paper, we explore the greedy pursuit model [56] for optimizing the parameters in (7). The advantage of this method is that it can significantly balance both complexity and accuracy. By optimizing \mathbf{U} , \mathbf{V} , \mathbf{S} , we take the gradient of the cost function with respect to these parameters and set it to 0. Starting with \mathbf{U} , we have

$$\begin{aligned} \frac{\partial \|\mathbf{Y}' - \mathbf{U}\mathbf{V} - \mathbf{S}\|_F^2 + \lambda \|\text{vec}(\mathbf{S})\|_1}{\mathbf{U}} &= (\mathbf{Y}' - \mathbf{U}\mathbf{V} - \mathbf{S}) \mathbf{V}^T \\ (\mathbf{Y}' - \mathbf{U}\mathbf{V} - \mathbf{S}) \mathbf{V}^T &= 0 \\ (\mathbf{Y}' - \mathbf{S}) \mathbf{V}^T - \mathbf{U}\mathbf{V}\mathbf{V}^T &= 0 \\ \mathbf{U}_k &= (\mathbf{Y}' - \mathbf{S}) \mathbf{V}_{k-1}^T (\mathbf{V}_{k-1} \mathbf{V}_{k-1}^T)^{-1}. \end{aligned} \quad (8)$$

Note subscript in k denotes the variable in the k th iterate. Next, we consider \mathbf{V}

$$\begin{aligned} \frac{\partial \|\mathbf{Y}' - \mathbf{U}\mathbf{V} - \mathbf{S}\|_F^2 + \lambda \|\text{vec}(\mathbf{S})\|_1}{\partial \mathbf{V}} &= \mathbf{U}^T (\mathbf{Y}' - \mathbf{U}\mathbf{V} - \mathbf{S}) \\ \mathbf{U}^T (\mathbf{Y}' - \mathbf{U}\mathbf{V} - \mathbf{S}) &= 0 \\ \mathbf{U}^T (\mathbf{Y}' - \mathbf{S}) - \mathbf{V}\mathbf{U}^T \mathbf{U} &= 0 \\ \mathbf{V}_k &= (\mathbf{U}_{k-1}^T \mathbf{U}_{k-1})^{-1} \mathbf{U}_{k-1}^T (\mathbf{Y}' - \mathbf{S}) \end{aligned} \quad (9)$$

Finally, we consider \mathbf{S}

$$\begin{aligned} \frac{\partial \|\mathbf{Y}' - \mathbf{U}\mathbf{V} - \mathbf{S}\|_F^2 + \lambda \|\text{vec}(\mathbf{S})\|_1}{\partial \mathbf{S}} &= (\mathbf{Y}' - \mathbf{U}\mathbf{V} - \mathbf{S}) + \lambda \\ (\mathbf{Y}' - \mathbf{U}\mathbf{V} - \mathbf{S}) + \lambda &= 0 \\ \mathbf{S}_k &= \mathbf{S}_\lambda (\mathbf{Y}' - \mathbf{U}_k \mathbf{V}_k) \end{aligned} \quad (10)$$

where \mathbf{S}_λ is an element-wise soft thresholding operator with λ threshold such that $\mathbf{S}_\lambda \mathbf{Y}' = \{\text{sgn}(\mathbf{Y}'_{mn}) \max(|\mathbf{Y}'_{mn}| - \lambda, 0)\}$. In this work, λ is selected by exploring

the heuristic approach to get the optimal threshold. We will treat this in two cases. For the case where \mathbf{S} is positive, the differentiation of $\text{abs}(\mathbf{S})$ results in unity. This allows λ to be incorporated into the solution to render extraction of sparse pattern. For the special case of \mathbf{S} is zero, even though this point is nondifferentiable, it does not prevent the development of the proposed algorithm. The reason is because at this point ($\mathbf{S} = \mathbf{0}$), the image is already sparse and there is no further need to impose lambda into the solution.

For computation efficiency [57], we investigate the product of $\mathbf{U}_k \mathbf{V}_k$, this leads to $\mathbf{U}_k \mathbf{V}_k = \mathbf{U}_k (\mathbf{U}_k^T \mathbf{U}_k)^{-1} \mathbf{U}_k^T (\mathbf{Y}' - \mathbf{S}) = \mathbf{P}_{\mathbf{U}_k} (\mathbf{Y}' - \mathbf{S})$. This implies that the product $\mathbf{U}_k \mathbf{V}_k$ equals to the orthogonal projection of $(\mathbf{Y}' - \mathbf{S})$ onto the column space of \mathbf{U}_k . According to (8), the column space of \mathbf{U}_k can be represented by arbitrary orthonormal basis for the columns of $(\mathbf{Y}' - \mathbf{S}) \mathbf{V}_{k-1}^T$. For example, we can compute it as \mathbf{Q} via fast QR decomposition $\mathbf{QR} = QR((\mathbf{Y}' - \mathbf{S}) \mathbf{V}_{k-1}^T)$. In this case, the product $\mathbf{U}_k \mathbf{V}_k$ can be equivalently computed as $\mathbf{U}_k \mathbf{V}_k = \mathbf{P}_{\mathbf{Q}} (\mathbf{Y}' - \mathbf{S}) = \mathbf{Q} \mathbf{Q}^T (\mathbf{Y}' - \mathbf{S})$. Therefore, \mathbf{U}_k and \mathbf{V}_k in (8) can be replaced by \mathbf{Q} and $\mathbf{Q}^T (\mathbf{Y}' - \mathbf{S})$, respectively. This gives a faster updating procedure. In addition, the proposed method invokes the updates in (8) with a greedy incremental rank r for both \mathbf{U} and \mathbf{V} . In particular, it starts from a $\mathbf{V} \in \mathbb{R}^{r_0 \times N}$ with a small integer r_0 , iterates (8) and (9) for K times, and then augment the rank of \mathbf{V} to $r_1 = r_0 + \Delta r$ by adding Δr extra rows to \mathbf{V} , where Δr is the rank step size. In the proposed model, the Δr rows are selected greedily as the top Δr row basis on which the object decreases fastest. Accordingly, they maximize the magnitude of the partial derivative of the object with respect to \mathbf{UV} , which is basis on which the object decreases fastest. Namely

$$\frac{\partial \|\mathbf{Y}' - \mathbf{UV} - \mathbf{S}\|_F^2}{\partial \mathbf{V}} = \mathbf{Y}' - \mathbf{UV} - \mathbf{S}. \quad (11)$$

Hence the Δr rows are the top Δr right singular vectors of the fat matrix $\mathbf{U}^T (\mathbf{Y}' - \mathbf{UV} - \mathbf{S})$, which can be quickly obtained by a small SVD and The rank r stops augmenting when reaching certain error tolerance. In the proposed model, the top r_i row basis are successfully obtained when optimizing \mathbf{V} of $r_i + \Delta r$ rows. The essential task of the updates is to optimize the added Δr rows, while the first r_i rows take part in the update merely for keep the incoherence between rows. Therefore, it converges faster than simultaneously optimizing the whole r rows. In addition, the newly added Δr rows are initialized as the fastest decreasing directions. This repeatedly increases the rank until a sufficiently small decomposition error is achieved. The rank of the low-rank component is adaptively estimated and does not rely on initial estimation. The specific steps can be summarized in Table I.

IV. EXPERIMENT SETUP

A. IT Experimental Platform

The experimental setup is shown in Fig. 4(a). An Easyheat 224 from Cheltenham Induction Heating is used for coil excitation. The Easyheat has a maximum excitation power of 2.4 kW, a maximum current of 400 A_{rms} and an excitation frequency

TABLE I
THERMAL SPARSE PATTERN EXTRACTION

| |
|-----------------------------------------------------------------------------------------------------------------------------------|
| Input: matrix representation of first derivative of ECPT thermal video \mathbf{Y}' (Inductive phase one is selected) |
| rank step size Δr ; power K ; tolerance τ ; sparse term λ |
| Output: thermal low rank pattern \mathbf{UV} and sparse pattern \mathbf{S} |
| Procedure: |
| Initialize: $\mathbf{V} \in \mathbb{R}^{r_0 \times N}$ and \mathbf{S} |
| while residual error $< \tau$ |
| for $k=1: K$ |
| $\mathbf{U}_k = \mathbf{Q}, QR((\mathbf{Y}' - \mathbf{S}_{k-1}) \mathbf{V}_{k-1}^T) = \mathbf{QR}$ |
| $\mathbf{V}_k = \mathbf{Q}^T (\mathbf{Y}' - \mathbf{S}_{k-1})$ |
| $\mathbf{S}_k = \mathbf{S}_\lambda (\mathbf{Y}' - \mathbf{U}_k \mathbf{V}_k)$ |
| end |
| Calculate the top Δr right singular vectors \mathbf{v} |
| of $\frac{\partial \ \mathbf{Y}' - \mathbf{UV} - \mathbf{S}\ _F^2}{\partial \mathbf{V}} = \mathbf{Y}' - \mathbf{UV} - \mathbf{S}$ |
| Set $\mathbf{V} := [\mathbf{V}, \mathbf{v}]$ |
| end |

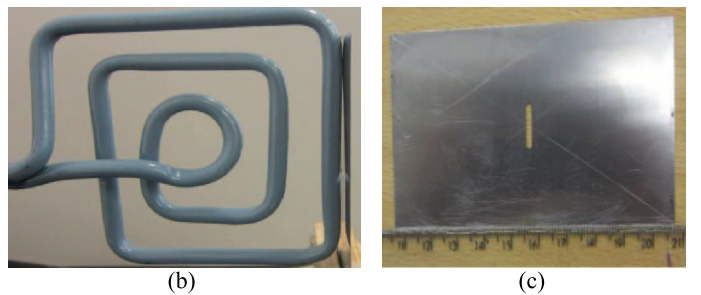
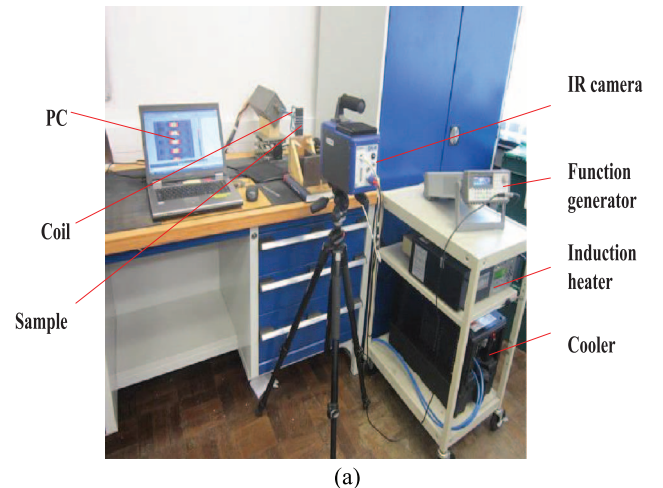


Fig. 4. (a) IT system. (b) Excitation coil. (c) Steel test sample.

range of 150–400 kHz (380 A_{rms}, and power is about 2.17 kW, and 256 kHz are used in this study). The system has a quoted rise time (from the start of the heating period to full power) of 5 ms, which was verified experimentally. Water cooling of coil is implemented to counteract direct heating of the coil. The IR camera, SC7500 is a Stirling cooled camera with a 320 × 256 array of 1.5–5 μm InSb detectors. This camera has a sensitivity of <20 mK and a maximum full frame rate of 383 Hz, with the

option to increase frame rate with windowing of the image. A rectangular coil is constructed to apply directional excitation. This coil is made of 6.35 mm high conductivity hollow copper tube. In the experiment, only one edge of the rectangular coil is used to stimulate EC to the underneath sample. In this study, the frame rate is 383 Hz, and 2 s videos are recorded in the experiments.

A steel sample (0.24 mm × 45 mm × 100 mm) with a slot of 10 mm length, 2 mm width is prepared (Fig. 4(c)). A 100 ms heating duration is selected for inspection, which is long enough to elicit an observable heat pattern. To simulate the lift-off variation in complex geometrical sample test, the steel sample is placed with a small angle against the coil [Fig. 4(b)].

B. Probability of Defect Detection

The POD of defect is defined as

$$\text{POD} = \frac{\text{TP}}{\text{TP} + \text{FN}} \quad (12)$$

where TP refers to true positive which represent the situation where the sample contains a defect and the method indicates a defect is present, and FN refers to false negative which represents the situation where the sample does not contain a defect and the method does not indicate a defect is present.

To validate the comparison results, structural similarity (SSIM) index measurement system is employed to measure the POD. It is a new index of image similarity measure. The SSIM theory presents that natural image signals are highly structured, the structure has a very strong correlation between pixels, and especially the spatial correlation of pixel is closest. The SSIM theory contains important information of an object structure in a visual scene. Indeed, the three components are combined to yield an SSIM given by

$$S(x, y) = f(l(x, y), c(x, y), s(x, y)) \quad (13)$$

where luminance comparison of two image (x, y) is defined as

$$l(x, y) = \frac{2u_x u_y + C_1}{u_x^2 + u_y^2 + C_1} \quad (14)$$

where u is mean intensity, C_1 is constant to avoid instability, when $u_x^2 + u_y^2$ is very close to zero. The contrast comparison is defined as

$$c(x, y) = \frac{2\sigma_x \sigma_y + C_2}{\sigma_x^2 + \sigma_y^2 + C_2} \quad (15)$$

where σ is standard deviation and the structure comparison function is defined as

$$s(x, y) = \frac{2\sigma_{xy} + C_3}{\sigma_x \sigma_y + C_3} \quad (16)$$

where σ_{xy} is correlation coefficient, C_2 and C_3 functions as same as C_1 , by combing all three factors, this gives the definition of SSIM [58], namely

$$\text{SSIM}(x, y) = \frac{(2u_x u_y + C_1)(2\sigma_{xy} + C_2)}{(u_x^2 + u_y^2 + C_1)(\sigma_x^2 + \sigma_y^2 + C_2)} \quad (17)$$

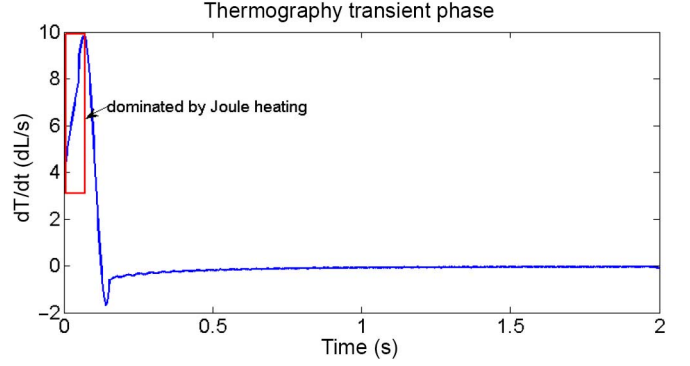


Fig. 5. First-order derivative of the transient response.

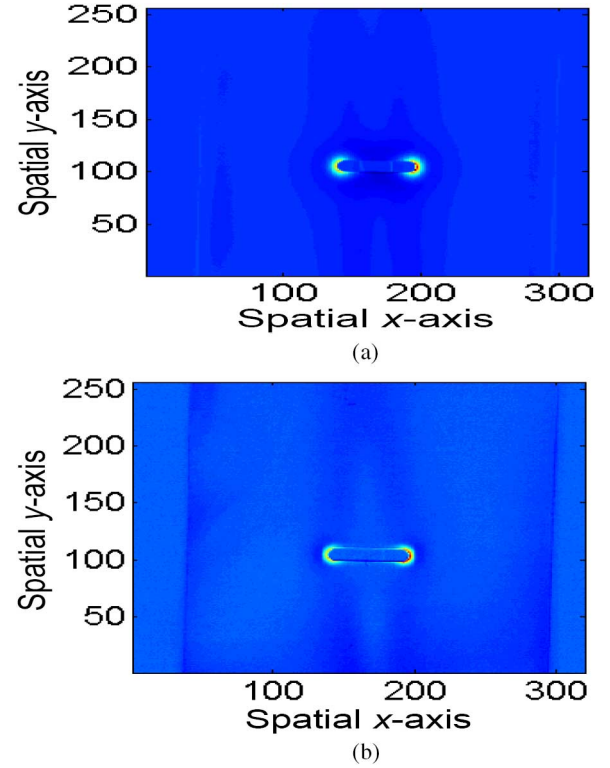


Fig. 6. (a) PCA of first derivative of whole thermal video. (b) PCA of first derivative of partially (phase one) thermal video.

V. RESULTS AND DISCUSSION

A. Influence of Phase Selection of IT

One example of raw inductive thermal image is shown in Fig. 1. The first derivative of transient response according (2) is shown in Fig. 5.

As can be seen clearly, the phase one can be interpreted within the rectangular box. In order to emphasize the importance of analyzing the phase selection, the comparison of defect pattern extraction by selecting first derivative of whole and partially (phase one) thermal video using general principle component analysis (PCA) using (5) by setting the number N_s of pattern basis to four. This selection is based on Monte Carlo approach where the process is repeated over 100 realizations within the range between the one up to 10 components and the

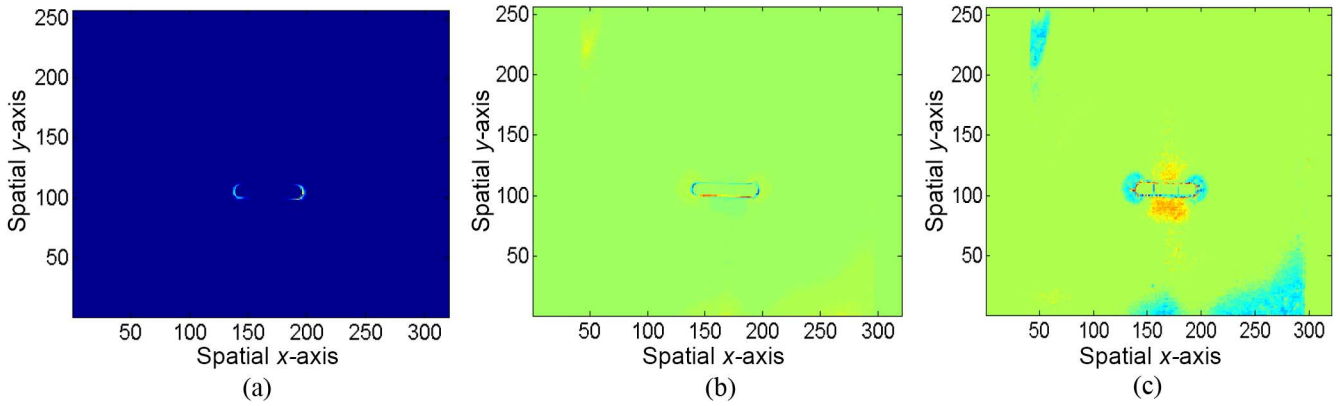


Fig. 7. Sparse pattern extraction results. (a) Proposed method. (b) Variational Bayesian sparse PCA with Gaussian sparse prior. (c) Bayesian sparse PCA based on MCMC with Bernoulli sparse prior.

selection of the four in order to obtain the optimal defect pattern extraction results.

In Fig. 6, both extraction results highlight the singular pattern around the crack tips. However, the PCA of first-order derivative of the “phase one” of the thermal video has enabled a heightened state of emphasis with higher resolution in the zone around the tips of the hot spots. In addition, this brings the benefit of lesser computations since only few thermal images are used. From the physics viewpoint, during the heating phase for a finite uniform thickness plate, a heat generation rate Q can be defined as the generated heat in unit time due to Joule heating, using the Cartesian coordinates (x, y) as follows:

$$Q = \sigma \left\{ \left(\frac{\partial \phi}{\partial x} \right)^2 + \left(\frac{\partial \phi}{\partial y} \right)^2 \right\} \quad (18)$$

where ϕ denotes the electric potential and σ electric conductivity. Since the two components of the electric current are expressed in terms of the derivatives of ϕ , heat generation rate Q theoretically goes to infinity at the crack tips. A resultant high temperature rising rate is generated in heating phase (i.e., crack tips) [25]. In the cooling phase, since there is no heating source, the variation of temperature T_{emp} in a finite uniform thickness plate is described as

$$\frac{\partial T_{\text{emp}}}{\partial t} = \frac{k}{\rho C_p} \left(\frac{\partial^2 T_{\text{emp}}}{\partial x^2} + \frac{\partial^2 T_{\text{emp}}}{\partial y^2} \right) \quad (19)$$

where t , ρ , C_p , and k denotes time, mass density, heat capacity, and thermal conductivity, respectively. It is clear that the temporal variation of temperature depends on the variation of spatial temperature. Fourier’s law of heat conduction states that the time rate of heat transfer through a material is proportional to the negative gradient in the temperature and to the cross section area of the material. For a uniform thickness plate used in this study, the cross section area is constant. Due to the singular areas around the slot tips, a high temperature gradient is generated while high EC density appears around the slot tips. During the shot time, the EC quickly rises from zero to maximum, retains at the steady state [25]. The heat diffusion does not play an obvious role as can be considered zero or a small value. This is the reason Fig. 6 indicates that the separated

TABLE II
SSIM RESULTS OF DIFFERENT METHODS

| Methods | POD | CPU time (s) |
|------------------------|------|--------------|
| PCA of the whole video | 0.84 | 169.5 |
| PCA on phase one | 0.91 | 15 |
| Proposed method | 0.99 | 3.5 |
| VBSPCA | 0.87 | 7.64 |
| MCMC sparse PCA | 0.68 | 1029 |

defect pattern place more emphasis on the crack tips where the heat diffusion does not significantly affect the heat distribution. Once the whole thermal procedure is processed, both heat diffusion and Joule heating are fused together in heat conduction procedure and the separated pattern assembles less in the crack tips.

B. Impact of Sparse Pattern Extraction

The sparse pattern extraction takes important role in quantitatively analyzing the cracks. We have compared the proposed method with the relative recent approach on sparse pattern extraction. These are the variational Bayesian sparse PCA with Gaussian sparse prior [49] and the robust Bayesian PCA with Bernoulli sparse prior [50]. The comparison is validated in both accuracy and computation complexity. In our proposed method, the sparse greedy model is explored for sparse pattern extraction which by adjusting proper sparse parameters that gives even better results and behaves much faster update procedure. Fig. 7 shows the extraction results.

In Fig. 7, by emphasizing the sparseness of solution, the edge of the hot spots on crack tips can be quantified and has benefited the quantitative sizing of the defect. The proposed method has successfully accentuated the expected sparse locations which indicate the hot spots of the crack tips. The variational Bayesian sparse PCA has also outlined the defect edge, however, with reference to the physics mechanism, the edges along the hot spots have been incorrectly detected (which should not present., Finally, the full Bayesian sparse PCA presents an inferior result which has emphasized both hot and cool areas as well as being interfered by noise. The above results are also confirmed by POD results as shown in Table II. The POD study

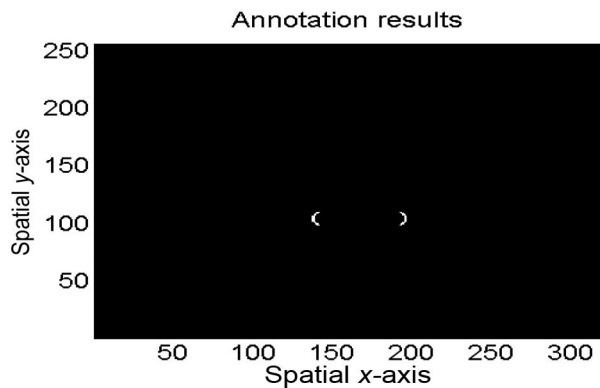


Fig. 8. Annotation results of crack edge.

is the comparison results between the referenced annotation with the extraction by algorithms. Fig. 8 shows the annotation results where the crack edge region is marked as “1” and the rest denoted as “0”.

Table II shows the comparison of the proposed method based on phase one thermal sparse pattern extraction. With human annotation results, the POD for all different methods, while a higher performance is attained by the proposed method with an average accuracy of 99%.

The variational Bayesian sparse PCA (VBSPCA) gives 87% while the worst result is obtained by MCMC sparse PCA which gives 68%. In addition, according to the computation time, the proposed method gives extremely low cost while it only take 0.07 s to achieve the extraction. This brings significantly benefits for industry online detection. VBSPCA requires more time about 7.64 s and the MCMC sparse PCA requires the most time about 1029 s. The reasons for these is attributed to both variational Bayesian and fully MCMC sparse PCA having to update the model parameters and hyperparameters in each iteration which cost extra computation complexity. Although the update parameters has advantages to bypass human intervention but it brings the drawbacks to the incorrect selection of prior distribution for the model parameters and/or convergence to local minima.

In terms of parameters selection of the proposed method, the parameter K and tolerance τ does not highly affect the extraction results. In general, it suffices to set $K = 1$ and $\tau = 10^{-3}$ and this has been validated using Monte–Carlo repeated experiment involving more than 100 independent trials. On the other hand, the sparse pattern extraction results is highly reliant on λ and Δr . First, for determining λ , which is based on model order selection where experiment is repeated by progressively increasing λ from 0.1 to 1 with step size is 0.1 (the deviation of the performance of all three experiments is $\text{POD} \pm 0.015$). Second, we have constructed another experiment by varying Δr . This parameter is a rank step size and should be integer. Our approach to determining Δr is based on model order selection where experiment is repeated by progressively increasing Δr from 1 to 5. For each experiment, we record the POD results and the overall obtained result is shown in Fig. 9. It is clearly seen from the figure the best POD result is obtained when $\Delta r = 2$. The POD results decrease gradually with the setting of $\Delta r > 2$.

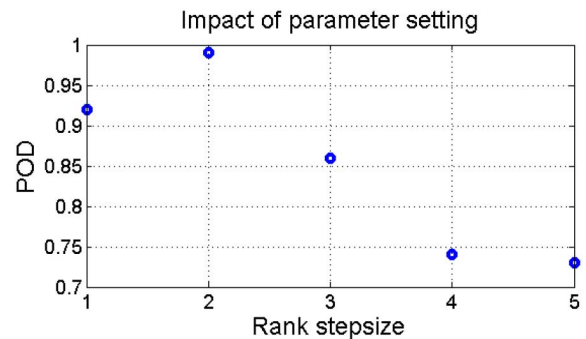


Fig. 9. Impact of parameter setting on POD results.

C. Impact of Detectability of Contamination Level of Material

The measurement set-up variation, relative humidity of the room, contamination level of material are valuable for the practical application of IT. Among the above three impact factors, the contamination level on the surface is the main factor to interface the results. In order to validate the proposed method in this situation, we have done the extra experiment. In the in-situ application, the materials under test (MUT) always have oil, coating, or an oxidation layer on the surface. This will change the thermal emissivity significantly. The variation can be used to detect the surface damage like rust or corrosion. However, the variation sometimes introduces illusory temperature inhomogeneity and results in false alarms. We paint the sample surface with black and shine strips which are equally spaced with 5 mm width. The shinning strips are the polished area while the black strips are the area sprayed with black paint. Both illustrate different level of emissivity. The emissivity of the black region is 1, which is the same for a blackbody. On the other hand, the emissivity of the shinning stainless steel surface is about 0.16. In this situation, once the test sample with the mixture of areas with strong emissivity gradient over another (e.g., black stains on the surface) and defect (e.g., slot which consists of cool and hot spots areas), the task of separating different thermal patterns becomes a very difficult challenge. Generally, the temperature of hot spots is three times higher than the cool area. However, the temperature of a black strip region can be as high as ten times higher than at the cool area due to the high emissivity. In this case, the hot spots around the slot tip cannot be observed and this directly reduces the probability of detecting the defects. Fig. 1(b) shows the temperature distribution at the end of heating (0.1 s) of testing sample in Fig. 10(a). Due to the high emissivity of the black area, there is no obvious high temperature region around the slot tips. The high temperature can only be observed at the black area above the coil. In addition, Fig. 10(c) shows the temperature distribution at the cooling phase (1.6 s). The high temperature still can only be observed at the black strip area because of both high emissivity and heat diffusion. The transient temperature behavior at different positions is shown in Fig. 11. Pos 1 is at the crack side with black strip (high emissivity), Pos 2 is at the black strip where the area is far away from the excitation, Pos 3 is at the crack tip

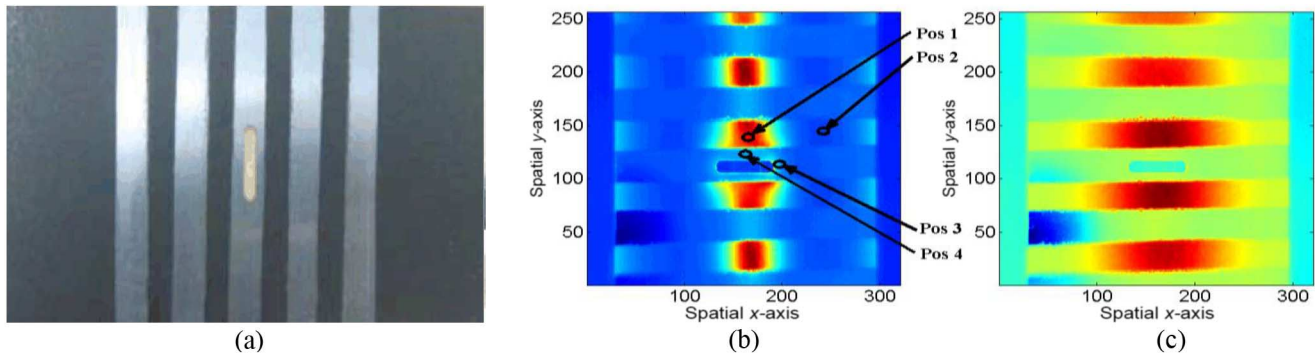


Fig. 10. (a) Painted steel sample with slot. (b) Infrared image at 0.1 s (the end of heating phase). (c) infrared image at 1.6 s (the cooling phase).

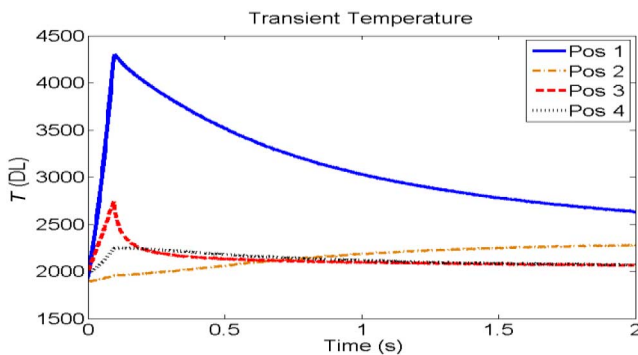


Fig. 11. Transient response of different positions.

with the shinning strip, Pos 4 is at the crack side with shinning strip above the coil.

As can be seen in Fig. 11, different position behaves with different temperature transient characteristics. However, Pos 1 as well as other similar black strip area (above the coil) exhibits extreme high temperature transient in both heating and cooling phase in which other thermal patterns have been over-shadowed and therefore, they cannot be distinguished. This issue is difficult to tackle in defect detection using the ECPT method where the hot spot around defect tips cannot be taken as an indicator of defects especially for small cracks. Notwithstanding this, it will lead to error when both black stain and cracks are present on the surface of the test sample.

Thus, the proposed method as well as compared methods will face a very challenging task to separate the hot spots. The following are the extraction results obtained from the proposed method, variational Bayesian sparse PCA, MCMC sparse Bayesian sparse PCA, and general PCA.

Fig. 12 shows that by emphasizing the sparseness of solution, the edge of the hot spots on crack tips can be quantified at the situation even under the influence of various emissivity levels. The proposed method has successfully extracted the expected sparse locations that indicate the hot spots of the crack tips. The variational Bayesian sparse PCA has also accurately outlined the defect edge but it still mixes with the emissivity interface and misses the informative points of left edge. The full Bayesian sparse PCA performs less satisfactorily and still retains a mixture of a large part of ambiguity. Finally,

the general PCA has enabled the extraction of the hot spots region but it has not fully reduced the emissivity interface. The above results are also supported by the POD results as shown in Table III. In terms of time consumption, the proposed method is very fast and takes only 0.11 s to render the extraction. The variational Bayesian sparse PCA also gives fast computation and takes about 8.34 s while the MCMC sparse PCA as well as the general PCA take a relatively longer time and requires about 1043 and 18 s, respectively.

D. Industrial Application: Micro-Natural Crack Detection

To verify the proposed system, thermal fatigue cracks (a 4.2-mm length crack) in steel blade are used for testing. A steel blade sample provided by Alstom is also investigated in this study (Figs. 13 and 14). In the blade, flaws are produced in-situ with controlled thermal fatigue loading. The flaws grow with natural thermal fatigue damage mechanism. In this study, one natural crack: 167BBB1361 is detected. The crack location is marked with red circles in Fig. 13. Crack 167BBB1361 is 4.2 mm length. A 200-ms heating duration is selected for inspection.

Fig. 15 shows the general NDT method using Penetrant Test (PT) image provided by Alstom and ECPT image at 0.1 s. In the PT image, the area of cracks is marked with red circle. The hot spots of crack can be visually identified, while the image is blurred. This phenomenon indicates that there exist cracks in the sample. However, the cracks are difficult to be quantified. Fig. 16 shows the proposed results.

From Fig. 16, it is clearly shown that the proposed method has not only accurately located the hot spots (crack tips) but also precisely sized the cracks. By comparing with human detection, the proposed method is a fully automatic and unsupervised defect detection method. The human detection seriously suffers from the lack of subjective evaluation and requires the manual selection of informative data for the defect detection. In addition, current defect characterization method in IT imaging system requires highly trained personnel. Therefore, automated defect characterization method is very desirable in future Intelligent Manufacturing and Maintenance. Moreover, the time cost is high since it requires manual detection. The detection results may not be repeatable. Additionally, considering the accuracy, this can be divided into two parts for

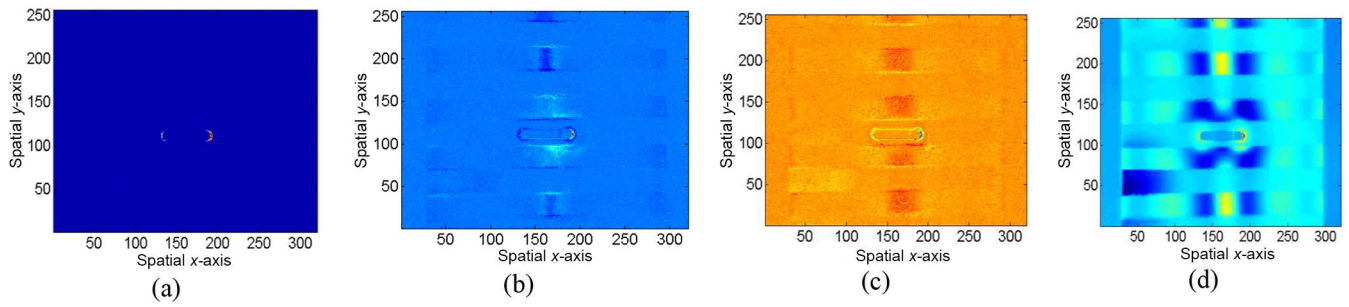


Fig. 12. Pattern extraction results. (a) Proposed method. (b) Variational Bayesian sparse PCA. (c) Bayesian sparse PCA based on MCMC. (d) General PCA.

TABLE III
SSIM RESULTS OF DIFFERENT METHODS

| Methods | POD | CPU time (s) |
|------------------|------|--------------|
| Proposed method | 0.97 | 5.5 |
| VBSPCA | 0.91 | 8.34 |
| MCMC sparse PCA | 0.63 | 1043 |
| PCA on phase one | 0.78 | 18 |

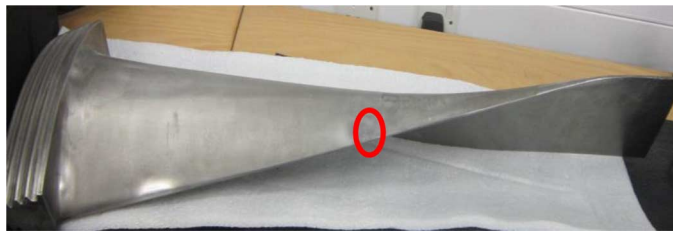


Fig. 13. Steel blade with thermal fatigue natural crack.

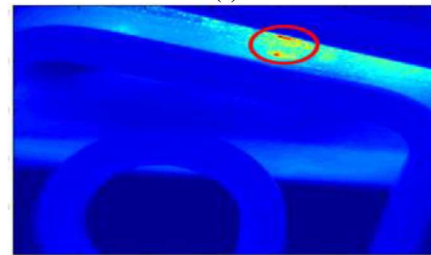


Fig. 14. ECPT test platform.

comparison: standard defect sample and natural defect. The human detection can render reasonably good accuracy in evaluating the defect based on regular sample. This is very sensible since the defect itself is introduced by human and we have the prior knowledge of the location and size of the defect. For natural cracks, it is extremely difficult for human detection because all the prior knowledge is unknown and the cracks are significantly small. This is shown in Fig. 13 where the size of the crack is only 1 mm wide. This is a very difficult task for human to detect the natural crack.

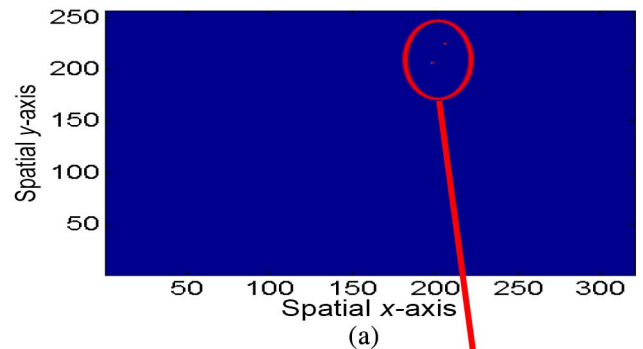


(a)

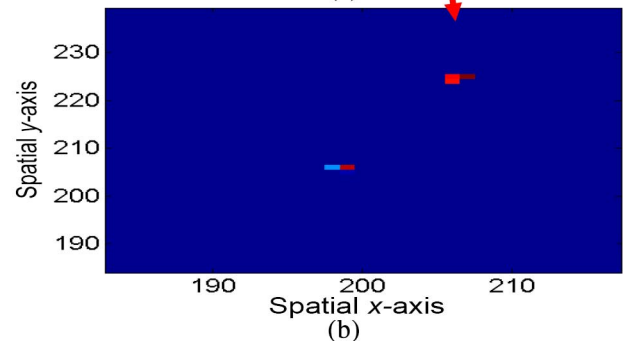


(b)

Fig. 15. Thermal fatigue natural cracks detection: length: 4.2 mm (a) PT image, (b) ECPT image at 0.1 s.



(a)



(b)

Fig. 16. (a) Thermal sparse pattern extraction results of natural crack. (b) Zoomed-in result (red circle).

The method ECPT is specific for conductive materials from CFRP composites to metals, and multilayer components including conductive parts. Its limitation is that it is invalid for nonconductive materials. However, by means of changing the inductive heater to lamp heater, ultrasound heater or laser heater, the proposed data analytics method and its physical interpretation are still valid for almost all thermal-conductive material.

VI. CONCLUSION AND FUTURE WORK

In this paper, inductive phase thermal sparse pattern extraction has been proposed for NDT&E. Both ECPT system and algorithm have been tested to validate the method. The physical interpretation of heat conduction phase of both Joule heating and heat diffusion has been conducted and the phase of Joule heating proved its efficiency for crack detection. The sparse pattern extraction method allows and emphasize sparse abnormal pattern such as hot spots around the crack tips to be extracted automatically for flaw contrast enhancement. The proposed method has been tested on both man-made and natural defects from industry. Future work will focus on samples with complex surface condition, e.g., roughness and emissivity variation. Complexity defects detection, e.g., subsurface defect in metallic material, impact damage, and delamination in carbon fiber structures will also be investigated.

REFERENCES

- [1] H. Gao, C. Ding, C. Song, and J. Mei, "Automated inspection of E-shaped magnetic core elements using K-tSL-center clustering and active shape models," *IEEE Trans. Ind. Informat.*, vol. 9, no. 3, pp. 1782–1789, Aug. 2013.
- [2] W. C. Li and D. M. Tsai, "Defect inspection in low-contrast LCD images using hough transform-based nonstationary line detection," *IEEE Trans. Ind. Informat.*, vol. 7, no. 1, pp. 136–147, Feb. 2011.
- [3] X. L. Bai, Y. M. Fang, W. S. Lin, L. P. Wang, and B. F. Ju, "Saliency-based defect detection in industrial images by using phase spectrum," *IEEE Trans. Ind. Informat.*, vol. 10, no. 4, pp. 2135–2145, Nov. 2014.
- [4] G. Acciani, G. Brunetti, and G. Fornarelli, "Application of neural networks in optical inspection and classification of solder joints in surface mount technology," *IEEE Trans. Ind. Informat.*, vol. 2, no. 3, pp. 200–209, Aug. 2006.
- [5] D.-M. Tsai, I.-Y. Chiang, and Y.-H. Tsai, "A shift-tolerant dissimilarity measure for surface defect detection," *IEEE Trans. Ind. Informat.*, vol. 8, no. 1, pp. 128–137, Feb. 2012.
- [6] A. Picon, O. Ghita, P. F. Whelan, and P. M. Iriando, "Fuzzy spectral and spatial feature integration for classification of nonferrous materials in hyperspectral data," *IEEE Trans. Ind. Informat.*, vol. 5, no. 4, pp. 483–494, Nov. 2009.
- [7] Y. Si, J. Mei, and H. Gao, "Novel approaches to improve robustness, accuracy and rapidity of iris recognition systems," *IEEE Trans. Ind. Informat.*, vol. 8, no. 1, pp. 110–117, Feb. 2012.
- [8] B. Gao, H. Zhang, W. L. Woo, G. Y. Tian, L. Bai, and A. Yin, "Smooth nonnegative matrix factorization for defect detection using microwave non-destructive testing and evaluation," *IEEE Trans. Instrum. Meas.*, vol. 63, no. 4, pp. 923–934, Apr. 2014.
- [9] D. M. Tsai and J. Y. Luo, "Mean shift-based defect detection in multicrystalline solar wafer surfaces," *IEEE Trans. Ind. Informat.*, vol. 7, no. 1, pp. 125–135, Feb. 2011.
- [10] X. P. Maldague, *Theory and Practice of Infrared Technology for Nondestructive Testing*. Hoboken, NJ, USA: Wiley, 2001.
- [11] P. Broberg, "Surface crack detection in welds using thermography," *NDT E Int.*, vol. 57, pp. 69–73, 2013.
- [12] R. Yang, Y. He, B. Gao, and G. Y. Tian, "Inductive pulsed phase thermography for reducing or enlarging the effect of surface emissivity variation," *Appl. Phys. Lett.*, vol. 105, no. 18, p. 184103, 2014.
- [13] B. Gao, A. Yin, G. Tian, and W. L. Woo, "Thermography spatial-transient-stage mathematical tensor construction and material property variation track," *Int. J. Therm. Sci.*, vol. 85, pp. 112–122, 2014.
- [14] H. Yang, B. Gao, G. Tian, W. Ren, and W. L. Woo, "Transient-spatial pattern mining of eddy current pulsed thermography using wavelet transform," *Chin. J. Mech. Eng.*, vol. 27, no. 4, pp. 768–778, 2014.
- [15] B. Oswald-Tranta and G. Wally, "Thermo-inductive surface crack detection in metallic materials," in *Proc. 9th Eur. Conf. NDT*, Berlin, Germany, 2006.
- [16] G. Zenzinger, J. Bamberg, W. Satzger, and V. Carl, "Thermographic crack detection by eddy current excitation," *NDT E Int.*, vol. 22, no. 2-3, pp. 101–111, 2007.
- [17] B. Weekes, D. P. Almond, P. Gawley, and T. Barden, "Eddy-current induced thermography-probability of detection study of small fatigue cracks in steel, titanium and nickel-based superalloy," *NDT E Int.*, vol. 49, pp. 47–56, 2012.
- [18] Y. He *et al.*, "Impact evaluation in carbon fiber reinforced plastic (CFRP) laminates using eddy current pulsed thermography," *Compos. Struct.*, vol. 109, pp. 1–7, 2014.
- [19] Y. He, G. Y. Tian, M. Pan, D. Chen, and H. Zhang, "An investigation into eddy current pulsed thermography for detection of corrosion blister, corrosion science," *Corros. Sci.*, vol. 78, pp. 1–6, 2014.
- [20] J. Wilson, G. Y. Tian, I. Mukriz, and D. Almond, "PEC thermography for imaging multiple cracks from rolling contact fatigue," *NDT E Int.*, vol. 44, pp. 505–512, 2011.
- [21] L. Cheng, B. Gao, G. Y. Tian, W. L. Woo, and G. Berthiau, "Impact damage detection and identification using eddy current pulsed thermography through integration of PCA and ICA," *IEEE Sensors J.*, vol. 14, no. 5, pp. 1655–1663, May 2014.
- [22] X. Maldague and S. Marinetti, "Pulse phase infrared thermography," *J. Appl. Phys.*, vol. 79, no. 5, pp. 2694–2698, 1996.
- [23] K. Chatterjee and S. Tuli, "Image enhancement in transient lock-in thermography through time series reconstruction and spatial slope correction," *IEEE Trans. Instrum. Meas.*, vol. 61, no. 4, pp. 1079–1089, Apr. 2012.
- [24] S. Marinetti *et al.*, "Statistical analysis of IR thermographic sequences by PCA," *Infrared Phys. Technol.*, vol. 46, pp. 85–91, 2004.
- [25] A. Hyvarinen, J. Karhunen, and E. Oja, *Independent Component Analysis and Blind Source Separation*. Hoboken, NJ, USA: Wiley, 2001, pp. 20–60.
- [26] B. Gao, L. Bai, G. Y. Tian, W. L. Woo, and Y. Cheng, "Automatic defect identification of eddy current pulsed thermography using single channel blind source separation," *IEEE Trans. Instrum. Meas.*, vol. 63, no. 4, pp. 913–922, Apr. 2014.
- [27] C. Févotte, "Majorization-minimization algorithm for smooth Itakura-Saito nonnegative matrix factorization," in *Proc. IEEE Int. Conf. Acoust. Speech Signal Process. (ICASSP)*, 2011, pp. 1980–1983.
- [28] B. Gao, L. Bai, W. L. Woo, and G. Tian, "Thermography pattern analysis and separation," *Appl. Phys. Lett.*, vol. 104, no. 251902, 5 pp., 2014, doi: 10.1063/1.4884644.
- [29] M. Elad, *Sparse and Redundant Representations: From Theory to Applications in Signal and Image Processing*. New York, NY, USA: Springer, 2010.
- [30] J.-L. Starck, F. Murtagh, and J. Fadili, *Sparse Image and Signal Processing: Wavelets, Curvelets, Morphological Diversity*. Cambridge, U.K., 2010.
- [31] E. Candès and M. Wakin, "People hearing without listening: An introduction to compressive sampling," *IEEE Signal Process. Mag.*, vol. 25, no. 2, pp. 21–30, Mar. 2008.
- [32] M. J. Fadili, J.-L. Starck, and F. Murtagh, "Inpainting and zooming using sparse representations," *Comput. J.*, vol. 52, pp. 64–79, 2009.
- [33] Z. Li, J. Liu, Y. Yang, X. Zhou, and H. Lu, "Clustering-guided sparse structural learning for unsupervised feature selection," *IEEE Trans. Knowl. Data Eng. (TKDE)*, vol. 26, no. 9, pp. 2138–2150, Sep. 2014.
- [34] B. Gao, W. L. Woo, and S. S. Dlay, "Variational Bayesian regularized two-dimensional nonnegative matrix factorization," *IEEE Trans. Neural Netw. Learn. Syst.*, vol. 23, no. 5, pp. 703–716, May 2012.
- [35] B. Gao, W. L. Woo, and S. S. Dlay, "Adaptive sparsity non-negative matrix factorization for single channel source separation," *IEEE J. Sel. Topics Signal Process.*, vol. 5, no. 5, pp. 1932–4553, Jun. 2011.
- [36] B. Gao, W. L. Woo, and S. S. Dlay, "Unsupervised single channel separation of non-stationary signals using Gammatone filterbank and Itakura-Saito nonnegative matrix two-dimensional factorizations," *IEEE Trans. Circuits Syst. I*, vol. 60, no. 3, pp. 662–675, Mar. 2013.
- [37] J.-L. Starck, J. Fadili, and F. Murtagh, "The undecimated wavelet decomposition and its reconstruction," *IEEE Trans. Image Process.*, vol. 16, no. 2, pp. 297–309, Feb. 2007.

- [38] M. J. Fadili and J.-L. Starck, "Curvelets and ridgelets," in *Encyclopedia of Complexity and System Science*. New York, NY, USA: Springer, 2008.
- [39] M. Aharon, M. Elad, and A. Bruckstein, "K-SVD: An algorithm for designing overcomplete dictionaries for sparse representation," *IEEE Trans. Signal Process.*, vol. 54, no. 11, pp. 4311–4322, Nov. 2006.
- [40] M. Zibulevski, "Blind source separation with relative Newton method," in *Proc. Ind. Compon. Anal. (ICA)*, 2003, pp. 897–902.
- [41] J. Kruskal, "Greedy algorithm for the minimum spanning tree problem," in *Proc. Amer. Math. Soc.*, 1956, pp. 48–50.
- [42] K. Papadimitriou and K. Steiglitz, *Combinatorial Optimization: Algorithms and Complexity*. Englewood Cliffs, NJ, USA: Prentice-Hall, 1982.
- [43] J. Tropp and A. Gilbert, "Signal recovery from random measurements via orthogonal matching pursuit," *IEEE Trans. Inf. Theory*, vol. 53, no. 12, pp. 4655–4666, Dec. 2007.
- [44] D. Needell and R. Vershynin, "Uniform uncertainty principle and signal recovery via regularized orthogonal matching pursuit," *Found. Comput. Math.*, vol. 9, no. 3, pp. 317–334, Jun. 2009.
- [45] B. Gao, W. L. Woo, and L. C. Khor, "Cochleagram-based audio pattern separation using two-dimensional non-negative matrix factorization with automatic sparsity adaptation," *J. Acoust. Soc. Am.*, vol. 135, no. 3, pp. 1171–1185, 2014.
- [46] N. Tengtrairat, B. Gao, W. L. Woo, and S. S. Dlay, "Single-channel blind separation using pseudo-stereo mixture and complex 2-D histogram," *IEEE Trans. Neural Netw. Learn. Syst.*, vol. 24, no. 11, pp. 1722–1735, Nov. 2013.
- [47] J. Bobin, J.-L. Starck, M. J. Fadili, and Y. Moudden, "Sparsity and morphological diversity in blind source separation," *IEEE Trans. Image Process.*, vol. 16, no. 11, pp. 2662–2674, Nov. 2007.
- [48] E. J. Candès, X. Li, Y. Ma, and J. Wright, "Robust principal component analysis?," *J. ACM (JACM)*, vol. 58, no. 3, 39 pp., May 2011, article no. 11.
- [49] Z. Lin, A. Ganesh, J. Wright, L. Wu, M. Chen, and Y. Ma, "Fast convex optimization algorithms for exact recovery of a corrupted low-rank matrix," *Int. Workshop Comput. Adv. MultiSens. Adapt. Process.*, Dec. 2009, submitted for publication.
- [50] S. D. Babacan, M. Luessi, R. Molina, and A. K. Katsaggelos, "Sparse bayesian methods for low-rank matrix estimation," *IEEE Trans. Signal Process.*, vol. 60, no. 8, pp. 3964–3977, Aug. 2012.
- [51] X. Ding, L. He, and L. Carin, "Bayesian robust principal component analysis," *IEEE Trans. Image Process.*, vol. 20, no. 12, pp. 3419–3430, Dec. 2011.
- [52] Y. He, M. Pan, D. Chen, G. Tian, and H. Zhang, "Eddy current step heating thermography for quantitatively evaluation," *Appl. Phys. Lett.*, vol. 103, p. 194101, 2013.
- [53] A. Yin, B. Gao, G. Y. Tian, W. L. Woo, and K. Li, "Physical interpretation and separation of eddy current pulsed thermography," *J. Appl. Phys.*, vol. 113, p. 064101, 2013, doi: 10.1063/1.4790866.
- [54] B. Gao, W. L. Woo, and B. W.-K. Ling, "Machine learning source separation using maximum a posteriori nonnegative matrix factorization," *IEEE Trans. Cybern.*, vol. 44, no. 7, pp. 1169–1179, Jul. 2014.
- [55] B. Gao, W. L. Woo, and S. S. Dlay, "Single channel source separation using EMD-subband variable regularized sparse features," *IEEE Trans. Audio Speech Lang. Process.*, vol. 19, no. 4, pp. 961–976, May 2011.
- [56] J. Demmel and W. Kahan, "Accurate singular values of bidiagonal matrices," *SIAM J. Sci. Stat. Comput.*, vol. 11, pp. 873–912, 1990.
- [57] J. Tropp, A. Gilbert, and M. Strauss, "Algorithms for simultaneous sparse approximations—Part I: Greedy pursuit," *Signal Process.*, vol. 86, pp. 572–588, 2006.
- [58] T. Zhou and D. Tao, "Greedy bilateral sketch, completion & smoothing," in *Proc. JMLR Workshop Conf.*, 2013, vol. 31, pp. 650–658.
- [59] Z. Wang, A. C. Bovik, H. R. Sheikh, and E. P. Simoncelli, "Image quality assessment: From error visibility to structural similarity," *IEEE Trans. Image Process.*, vol. 13, no. 4, pp. 600–612, Apr. 2004.



Bin Gao (M'12–SM'14) received the B.S. degree in communications and signal processing from Southwest Jiao Tong University, Leshan, China, in 2005, the M.Sc. degree in communications and signal processing (with distinction), in 2007, and the Ph.D. degree in research of blind source separation and statistic signal processing from Newcastle University, Newcastle Upon Tyne, U.K., in 2011.

From 2011 to 2013, he worked as a Research Associate on wearable acoustic sensor technology with Newcastle University. Currently, he is an Associate Professor with the School of Automation Engineering, University of Electronic

Science and Technology of China (UESTC), Chengdu, China. He is also a very active Reviewer for many international journals and long standing conferences. He has coordinated several research projects for the National Natural Science Foundation of China. His research interests include sensor signal processing, machine learning, social signal processing, nondestructive testing, and evaluation, and he actively publishes in these areas.



Wai Lok Woo (M'09–SM'11) received the B.Eng. degree (first class Hons.) in electrical and electronics engineering, and the Ph.D. degree in blind source separation and statistic signal processing from Newcastle University, Newcastle Upon Tyne, U.K. in 1993 and 1998, respectively.

Currently, he is a Senior Lecturer and Director of Operations with the School of Electrical and Electronic Engineering, Newcastle University. He has authored over 250 papers in various journals and international conference proceedings.

His research interests include mathematical theory, algorithms for nonlinear signal and image processing, machine learning for signal processing, data mining, blind source separation, multidimensional signal processing, and high-performance computational intelligence.

Dr Woo is currently an Associate Editor for several international journal and has served as a Lead Editor for journal special issues. He is a Member of the Institution Engineering Technology (IET). He was awarded the IEE Prize and the British Scholarship to continue his research work.



Yunze He (M'11) received the Ph.D. degree in nondestructive testing and evaluation from the College of Mechatronics, Engineering, and Automation, National University of Defense Technology (NUDT), Changsha, China, in 2012, and the Joint Ph.D. study from the School of Electrical, and Electronic Engineering, Newcastle University, Newcastle Upon Tyne, U.K., and NUDT, in 2012.

He is a Lecturer with NUDT. In the past five years, he has chaired or participated in about 20

projects including the National Natural Science Foundation of China, and the Engineering and Physical Sciences Research Council. He has authored more than 40 academic papers in journals and conferences, which have been cited more than 500 times in Google Scholar and have h-index of 12. His research interests include eddy current testing, thermography, and composite testing in the field of nondestructive testing and structural health monitoring.



Gui Yun Tian (M'01–SM'03) received the B.Sc. degree in metrology and instrumentation, and the M.Sc. degree in precision engineering from the University of Sichuan, Chengdu, China, in 1985 and 1988, respectively, and the Ph.D. degree in nondestructive testing and evaluation and computer vision from the University of Derby, Derby, U.K., in 1998.

From 2000 to 2006, he was a Lecturer, Senior Lecturer, Reader, Professor, and Head of the Group of Systems Engineering, respectively,

with the University of Huddersfield, West Yorkshire, U.K. Since 2007, he has been based at Newcastle University, Newcastle Upon Tyne, U.K., where he has been a Chair Professor in Sensor Technologies. Currently, he is also with the School of Automation Engineering, University of Electronic Science and Technology of China, Chengdu, China. He has coordinated several research projects from the Engineering and Physical Sciences Research Council, Royal Academy of Engineering and FP7, and in addition to this, he also has good collaboration with leading industrial companies such as Airbus, Rolls Royce, BP, nPower, and TWI, among others.